

ARTICLE OPEN

Transport mechanisms during the high-temperature oxidation of ternary γ/γ' Co-base model alloysMartin Weiser¹, Richard J. Chater², Barbara A. Shollock³ and Sannakaisa Virtanen^{1*}

Over a decade ago, γ' -strengthened Co-base alloys were introduced as potential replacement for conventional Ni-base Superalloys. Insufficient resistance against high-temperature oxidation restricts the number of possible applications. The present study contributes to the understanding of elementary mechanisms such as material transport during extensive oxide scale formation on γ/γ' Co-base alloys to explain their inferior oxidation behaviour. A clear dependency of the scale growth kinetics on W content and oxidation temperature is demonstrated by thermogravimetry and subsequent analysis of cross-sections. By means of electron backscattered diffraction (EBSD), the evolution of microstructures in the outer oxide layers were examined depending on the oxidation temperature. Sequential exposure of samples in $^{16}\text{O}_2$ - and $^{18}\text{O}_2$ -containing atmospheres proved counter-current material transport. The combination of focused ion beam (FIB) and secondary ion mass spectroscopy (SIMS) visualised the formation of new oxide phases mainly on the outer and inner interface of the oxide scale. An elaborate review of available transport paths for oxygen is given during the discussion of results. All experimental findings were combined to a coherent explanation of the inferior oxidation resistance of this relatively new class of high-temperature materials at temperatures above 800 °C.

npj Materials Degradation (2019)3:33

; <https://doi.org/10.1038/s41529-019-0096-z>

INTRODUCTION

Conventional Fe-, Ni- or Co-base alloys proved their suitability for various technical applications, especially during operation in harsh conditions at elevated temperatures. Due to their good mechanical performance, Ni-base Superalloys were unchallenged for decades as alloys that are used for turbine blades in sections of gas turbines where they withstand aggressive service conditions.¹ The strengthening by a cuboidal L1_2 (γ') phase that is coherently embedded in the (A1) matrix phase ensures the outstanding resistance against creep at high temperatures.^{2,3} In general, adequate durability in oxidising atmospheres is achieved by the addition of Al and Cr, to establish the formation of protective alumina and/or chromia scales.^{3,4} The systematic description of processes, such as material transport, which are essential for the growth of continuous, diffusion-limiting Al_2O_3 and Cr_2O_3 layers on various alloys, started over 50 years ago.^{5–7} Wagner^{5,8} repeatedly demonstrated that diffusion processes on the reaction front between oxide and substrate need to be elucidated, to explain or predict the growth of barrier layers in multi-element alloys. Nevertheless, there is still considerable research effort to unravel mechanistic details of the complex oxide scale growth on alumina-forming high-temperature alloys.^{9,10}

The in-service capability of Ni-base Superalloy is limited by their melting point and is therefore close to its maximum.¹¹ In 2006, the demonstration of a comparable strengthening (γ') phase $\text{Co}_3(\text{Al,W})$ in the ternary Co-Al-W system caused a continuously growing interest in Co-base Superalloys as potential alternative for Ni-base counterparts.¹² Due to the higher melting point of Co compared with that of Ni, the scientific community shared the hope that the design of alloys that might be capable of operating at even higher service temperatures could be mastered in the near future. Early studies on mechanical properties at temperatures above 800 °C delivered promising

results.^{13,14} However, at 900 °C, only insufficient resistance against oxidation was repeatedly reported.^{15–17} Interestingly, the formation of continuous alumina layers on the internal oxidation front (IOF) was observed in various polycrystalline Co-base model systems only at comparably low temperatures.^{15,18,19} This oxidation behaviour is contradictory to the scaling mode of Al-containing Ni-base alloy systems. At constant Al levels, Pettit²⁰ demonstrated significantly higher tendency for the transition from internal oxidation to the formation of a continuous Al_2O_3 layer with increasing temperatures.

For the description of the scaling mechanisms in the Co-Al-W model system, which lead to the development of barrier layers, especially at lower temperatures, detailed knowledge of transport processes during oxidation are essential. We have previously provided direct evidence for Al transport paths along γ channels in the two-phase microstructure of a ternary Co-Al-W alloy during early stages of scale formation at 900 °C.²¹ Due to preferential segregation of W in the γ' phase, the volume fraction of the matrix phase in a ternary Co-Al-W system directly depends on the overall W content.^{22,23} The importance of balanced elemental fluxes towards the IOF, which are depending on the alloy composition, for the formation of barrier layers in Co/Ni-base model alloys at 900 °C was recently discussed by two studies.^{24,25}

Two-stage tracer exchange experiments are established for drawing conclusions on elementary transport mechanisms during oxidation at high temperatures.^{26–29} After sequential exposure of samples in $^{16}\text{O}_2$ and $^{18}\text{O}_2$ atmospheres, secondary neutral mass spectroscopy (MS) or secondary ion MS (SIMS) is used to detect the location of newly grown ^{18}O -containing oxide. Visualisation of oxygen diffusion paths on mechanically polished cross-sections after tracer exchange experiments was demonstrated by Ooi et al.³⁰ The referred approach was recently also applied for Co/Ni-base model alloys.³¹ The described technique particularly benefits

¹Institute for Surface Science and Corrosion, Friedrich-Alexander-Universität Erlangen-Nürnberg (FAU), Martensstrasse 7, Erlangen, Germany. ²Department of Materials, Imperial College London, South Kensington, London SW7 2AZ, UK. ³Department of Engineering, King's College London, WC2R 2LS London, UK. *email: virtanen@ww.uni-erlangen.de

from the provided nanoscale lateral resolution in chemical data as well as imaging that is gained by the utilised gallium-ion focused ion beam (FIB). Due to the combination of the two data sets, tracer intensities can directly be attributed to specific morphological features in the complex oxide scales at a quality level that is hardly obtained by comparable studies.

In the present study, elementary oxidation mechanisms during the transient stages of scale growth between 800 °C and 900 °C on single-crystalline Co-Al-W alloys are elucidated. Despite the narrow (γ/γ') two-phase region in the ternary Co-Al-W system,¹² certain variations in the W levels are possible.²³ A nearly linear relation between γ' volume fraction and W content was reported.²³ Three ternary compositions with 9 at.% Al and alternating W levels of 7, 9 and 10 at.% were chosen to elucidate the impact of W and the γ' volume fraction during early stages ($t < 24$ h) of scale growth. The acronyms used in this study indicate the nominal W content of the respective single-crystal alloy. Oxide scales after thermogravimetry and two-stage tracer exchange experiments are analysed in detail. During the discussion, all acquired results on relevant elementary processes are supplemented by classical model predictions from literature.

RESULTS

Influence of W content

Mass gain data of ternary Co-base alloys continuously recorded during 24 h exposure in synthetic air between 800 °C and 900 °C are displayed in Fig. 1. Weight gains during isothermal oxidation of alumina-forming commercial Ni- or Fe-base high-temperature alloys that were investigated in a comparable temperature regime (< 1000 °C) were reported to stay considerably below 0.4 mg/cm³ even beyond 100 h of exposure.^{32–34} Compared with these studies, the increase in weight for all samples is substantial. The compositions with higher W contents exhibit significantly slower oxidation rates over the whole duration of experiments.

A detailed consideration of changing oxidation rates during exposure of a ternary Co-base model alloy with 9 at.% W at 900 °C were published in a previous study covering 100 h of scale growth.²¹ The length of transient oxidation kinetics with initially fast weight gain after the beginning of scale growth to overall slower oxidation kinetics strongly depends on the composition of the sample and the exposure temperature. A long transient period extending more than 15 h is apparent for 7Wsx. For higher W contents, the initial period shortens. In the case of 10Wsx, the slope of mass gain exhibits a first alteration after ~ 10 h. Thermogravimetry for 24 h of samples with 9 at.% W were also conducted at 800 °C and 850 °C. For lower temperatures, transitions in the reaction kinetics are less pronounced.

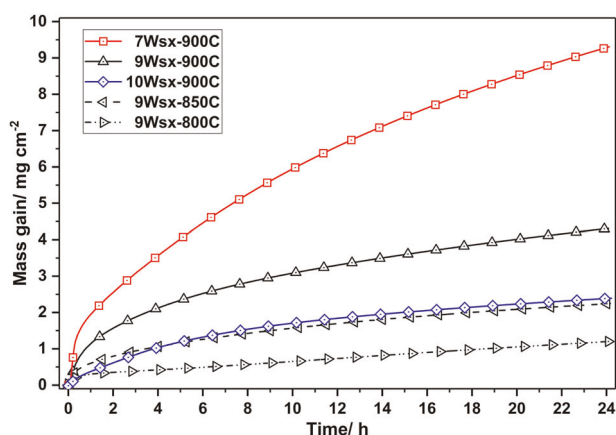


Fig. 1 Mass gain during 24 h oxidation between 800 °C and 900 °C in synthetic air

Furthermore, the samples demonstrate lower increase in weight during the experiment. The difference between the continuous data recorded at 900 °C and 850 °C exceeds the one detected between 850 °C and 800 °C by a factor of 2. The overall mass gain per surface area after 24 h exposure of 9Wsx at 850 °C reaches approximately the same value that was measured for the oxidation of 10Wsx at 900 °C. Transition in reaction kinetics of 9Wsx samples oxidised below 900 °C are less pronounced and will therefore not be considered in detail.

A comparison of backscattered electron (BSE) micrographs of oxide scales after 24 h exposure at 900 °C in synthetic air is provided in Fig. 2. All elucidated oxide scales on ternary Co-Al-W model alloys reveal three distinct layers.

On top of the initial alloy surface, an outer oxide layer (d_1) formed. This layer can be expected to consist almost completely of CoO. Below d_1 , an inner oxide layer (d_2) including a conglomerate of various oxide phases is clearly separated from the internal precipitation region (d_3). The narrow zone including the interface between the deepest formed oxide species and alloy is generally referred to as IOF. In comparison with the inner oxide layer, d_3 consists of dark Al₂O₃ precipitates embedded in the unoxidised matrix. For more detailed information, especially concerning microstructural features in the internal oxidation zone ($d_2 + d_3$), the reader is referred to our previous publications.^{21,35} Even though increasing W contents in the single-crystal samples leads to significantly higher γ' volume fractions (compare insets in Fig. 2), only a minor impact on the overall appearance of the multilayered oxide scales can be found. The micrograph taken from the cross-section of 10Wsx exhibits considerable amount of discontinuous alumina segments in the internal precipitation regions. Due to the slow lateral growth of these discontinuous alumina segments, they only provide a localised and hence insufficient barrier to oxygen transport. In other words, no diffusion-limiting scale sections were found in the set of ternary Co-base model alloys after 24 h thermogravimetry. Nevertheless, the individual thickness of distinguished scale regions is strongly dependent on the W level in the ternary system. The general trend of higher W contents leading to lower oxidation rates is also reflected in the dimensions of the individual layers.

At 900 °C, the evident decay of the initially high reaction kinetics to more moderate oxidation rates occurred for 9Wsx during the first 12 h of exposure (see Fig. 1). Alterations in the growth rates of the outer oxide layer can be one reason for these pronounced changes. For the growth of NiO, quantitative studies demonstrated that increasing grain size causes considerable changes in the overall rate constants.^{36,37} The outer oxide layer of ternary Co-base model alloys exhibited a coarse-grained microstructure after 100 h thermogravimetry at 900 °C in air.³⁵ In the following, the grain structure of d_1 , which developed on 9Wsx during exposure at 900 °C, is documented by electron backscattered diffraction (EBSD) measurements of the relevant scale sections. Due to the large interaction volume of the electron beam with the sample, the lateral resolution is restricted. As grain sizes above 1 μ m are expected, the chosen analysis method is sufficient to demonstrate the changes to the microstructure of d_1 . Inverse pole figure (IPF) maps of the CoO layer after 30 min, 1, 5 and 12 h of oxidation are provided in Fig. 3. Electron micrographs (not shown) that were observed in parallel with the recording of EBSD data indicated that regions without any signal or clear allocation to any grain orientation can be correlated to pores within the outer oxide layers (see also Fig. 2).

After 30 min oxidation, the outer oxide layer consists of many grains with a maximum diameter of ~ 5 μ m. Directly above the original alloy surface, a comparably thin (< 2 μ m) section of equally oriented small grains can be observed. Above this layer, significant porosity impedes the assignment of measurement spots to grain orientations. The size of grains that developed closer to the outer scale interface decreases. Already after 1 h oxidation, the centre of

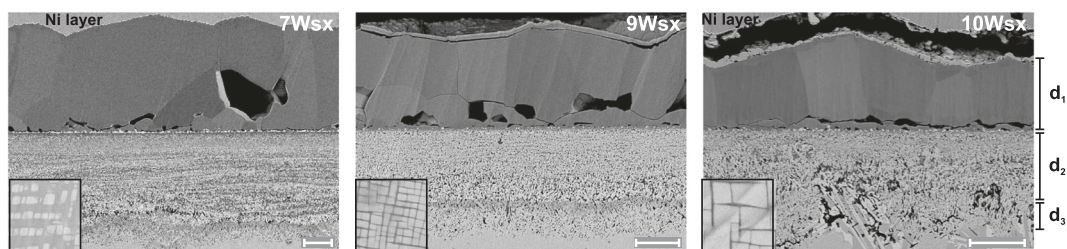


Fig. 2 BSE micrographs after 24 h oxidation at 900 °C in synthetic air. Scale bars, 10 μm. Insets demonstrate a 2 × 2 μm region of the unaffected two-phase microstructure

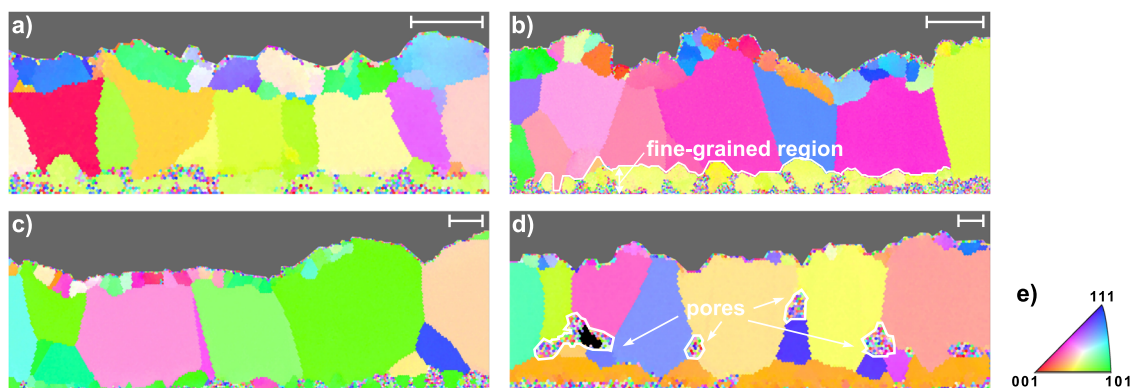


Fig. 3 IPF maps of externally grown CoO layers on 9Wsx. Displayed are representative sections of the outer oxide layer after (a) 30 min, (b) 1 h, (c) 5 h and (d) 12 h exposure at 900 °C in synthetic air. e Stereographic triangle for CoO. Scale bars, 5 μm

d_1 is dominated by columnar coarse grains. In the displayed oxide scale section after 5 h exposure, the overall fraction of the fine-grained outer region further decreases. The sample that was exposed for 12 h at 900 °C additionally exhibits comparably large pores between the columnar grains. At the outer scale interface, the nucleation and growth of new, small grains could only be observed to a minor extent. The zone of epitaxial grain above the original alloy surface demonstrates an increased thickness compared with the one detected in 9Wsx after 1 and 5 h oxidation.

In Fig. 4, IPF maps of all considered alloys after 24 h exposure in synthetic air at 900 °C are displayed. The size and structure of grains in the outer oxide layer of 9Wsx further coarsened between 12 and 24 h. For all three compositions, the displayed IPF maps exhibit regions of coarse grains that dominate d_1 . In the outer oxide layer that is found on faster oxidising samples with 7 and 9 at.% W, the columnar grains already reach to the outer scale interface. For the sample with the highest W level, growth of small grains on the outer region of d_1 is still evident.

Each sample exhibits comparably large pores between the columnar grains (see also Fig. 2). Following the general trend of slower reaction kinetics with higher W contents, the thickness of the epitaxial region of small grains above the original alloy surface decreases for 9Wsx and 10Wsx. Besides this fine-grained sections, no preferential orientation was observed in any CoO layer. As demonstrated in Fig. 1, oxidation kinetics of 9Wsx significantly decreases below 900 °C. Representative micrographs of samples with intermediate W content after 24 h exposure at 800 °C and 850 °C are displayed in Fig. 5a, b.

Specimens of 9Wsx that were oxidised for 24 h at 800 °C and 850 °C exhibit comparable morphological features, which were already apparent after scale growth at higher temperatures. The oxide scales can be distinguished in the above described three individual layers. As expected, the overall thickness of the scales decreases. The displayed part of the sample cross-section, which was exposed at 800 °C, includes a laterally spread alumina section

on the IOF (Fig. 5a). The outer oxide layer that is observed after 24 h exposure at 850 °C exhibits a higher degree of porosity. To verify whether growth of duplex scales can still be observed on ternary Co-base model alloys at 800 °C and 850 °C, further EBSD measurements were conducted. The determined IPF maps of the investigated oxide scales are displayed in Fig. 5c, d. After 24 h oxidation at temperatures below 900 °C, the outer oxide layers are not characterised by a duplex structure. Instead, the observed grain sizes are widely comparable in the two elucidated oxide scales. Neither a considerable epitaxial inner zone nor any preferred orientations are evident after exposure at lower temperatures. Nevertheless, all grains are slightly more extended into the growth direction, which indicates minor differences between the activation energies of nucleation and lattice expansion during grain growth. Finer grains on the outer oxide interface at temperatures below 900 °C lead to a less regular appearance of the scale surface.

Material transport between 800 °C and 900 °C

The previous results provide mainly information on the expansion of the outer oxide layer. Growth of d_1 can only be sustained by considerable diffusion of cations to the outer scale interface. To gain more detailed insights into the transport of material during the early stages of scale formation on ternary Co-base model alloys, two-stage oxidation experiments were conducted on this alloy series. By using the distinguishable stable oxygen isotopes ^{16}O and ^{18}O , the well-acclaimed technique delivers direct evidence for the transport paths of oxygen and provides supplementary information on the diffusion of cations during short-term exposure in the considered temperature window. Due to the complex nature of the internal oxidation zone, SIMS investigations are limited to the distribution of $^{16}\text{O}^-$ and $^{18}\text{O}^-$ in the scale. In contrast to the thermometric experiments in synthetic air, the atmosphere during the tracer exchange experiments was pure oxygen. The exposures were conducted at 200 mbar, to account for the altered conditions. To confirm that the resulting

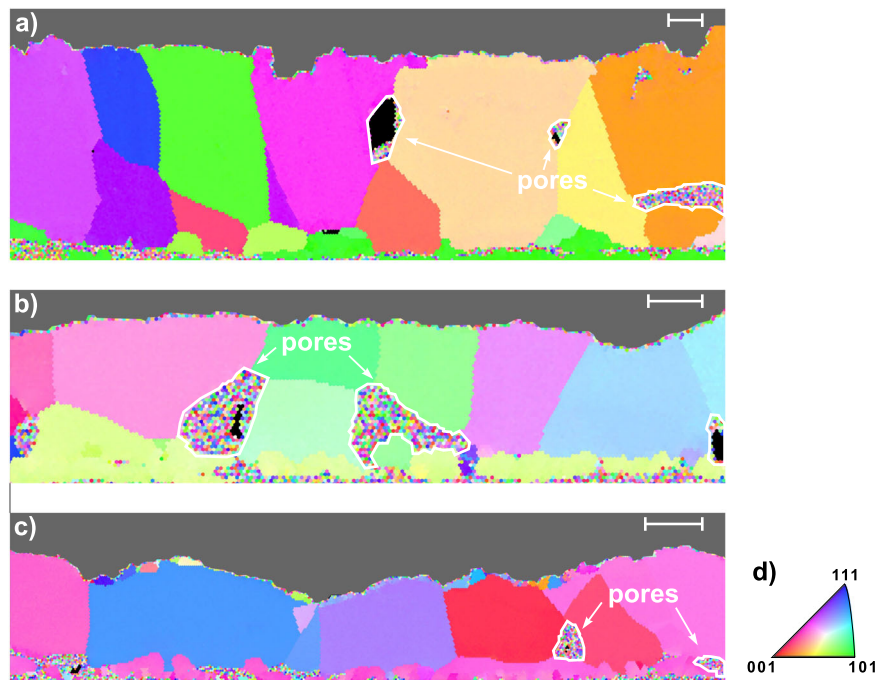


Fig. 4 IPF maps of externally grown CoO layers after 24 h exposure at 900 °C in synthetic air. Displayed are representative sections of the outer oxide layer on (a) 7Wsx, (b) 9Wsx and (c) 10Wsx. **d** Stereographic triangle for CoO. Scale bars, 10 μ m

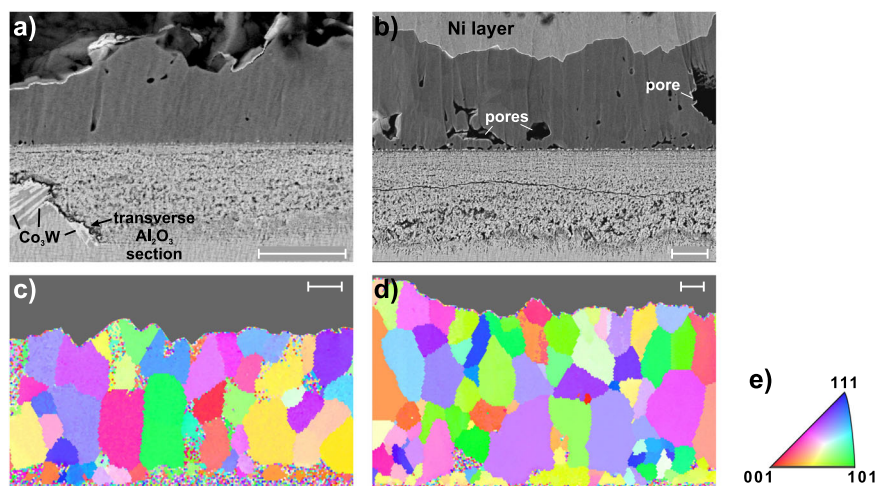


Fig. 5 BSE micrographs and corresponding IPF maps of d_1 after 24 h oxidation in synthetic air. Displayed are cross-sections after exposure at (a, c) 800 °C and (b, d) 850 °C. **e** Stereographic triangle for CoO. Scale bars, 5 μ m

oxide scales are comparable, individual layer thickness after each 24 h experiment of the present study are summarised in Fig. 6.

Each value represents the mean of five measurements. Standard deviations are given as error bars. By reviewing the data, a negligible influence of N_2 during the scale growth in the first 24 h exposure can be observed. The determined expansions of distinguished layers that were observed after 24 h oxidation in the different set-ups are consistent. Minor deviations between outer oxide scale thicknesses (d_1) formed in the different experimental set-ups can be seen for the samples that contain 10 at.% W. As the general tendency towards slower oxidation kinetics with increasing W contents remains unaffected from this scatter, results from both experimental approaches can be combined to one reliable study on mass transport mechanisms during scale growth on Co-Al-W systems.

To facilitate an easier allocation of tracer distribution to specific morphological features of the investigated oxide scales, the total positive secondary ion (SI) images of the analysed sample regions were recorded immediately prior to acquisition of SIMS maps. The same lateral resolution was used for both data sets. SI micrographs of representative oxide-scale cross-sections along with corresponding $^{18}O^-$ maps of ternary Co-base model alloys after 24 h tracer exchange experiments at 900 °C are demonstrated in Fig. 7.

Due to the changed contrast conditions in SI micrographs, d_3 appears less clear in the displayed cross-sections. However, closer examination reveals a particularly pronounced zone of Al_2O_3 precipitates for the sample that contains 10 at.% W. The distribution and size of pores in the outer oxide layers is widely comparable to the one obtained during thermogravimetric exposure.

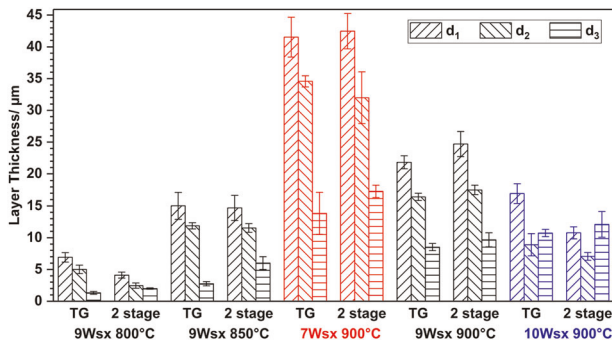


Fig. 6 Individual layer thicknesses of samples after 24 h exposure between 800 °C and 900 °C in synthetic air (TG) or 200 mbar oxygen (two-stage experiments). Error bars represent the SD of five measurements

The distribution of labelled $^{18}\text{O}^-$ after two-stage oxidation experiments revealed similar transport mechanisms for all considered ternary Co-base model alloys. At 900 °C, counter-current transport of reactants through the growing scale is evident. The amount of newly formed oxide phases during the second stage of the experiment is determined by the prevailing oxidation kinetics after 16 h and therefore also dependent on the W content (see also Fig. 6). Continuous outward diffusion of metal cations results in a distinctly demarcated region of labelled oxygen on the outer oxide interface. Furthermore, enrichment of ^{18}O isotopes is particularly evident around pores and cracks in d_1 of 9Wsx and 10Wsx. Due to the overall lower signal of $^{18}\text{O}^-$, which was measured for 7Wsx, labelled oxide in pores is less evident but also traceable (white circles in Fig. 7d). The sample with an intermediate W level of 9 at.% moreover exhibits a grain boundary in the outer oxide scale, which is characterised by an enrichment of newly formed oxide in its surrounding regions. Closer inspection of the outer oxide layer on 10Wsx also reveals grain boundaries that are decorated with ^{18}O (white arrows in Fig. 7f). At this stage, transport mechanisms for the penetration of oxygen to form new oxide at the scale/alloy interface are less clear. From the intermediate levels of $^{18}\text{O}^-$ signals in the inner oxide layer, also diffusion-driven transport through this layer might be inferred. The internal precipitation region (d_3) can be divided into two parts. In the upper regions, no considerable amounts of $^{18}\text{O}^-$ are evident. The localised high isotopic enrichment towards the IOF is not distributed over the whole length of d_3 after 24 h exposure at 900 °C.

Several authors suggested the usage of isotopic fractions (if_{18}) to eliminate unwanted influences that are caused by localised charging, instrumental factors or sample topography.^{29,38} As the dwell time for the acquisition of $^{16}\text{O}^-$ and $^{18}\text{O}^-$ maps was varied, a correction factor is needed to reach comparable conditions for accurate pointwise calculation of if_{18} . The relative tracer enrichment during the second oxidation stage can be determined by normalising the calculated if_{18} values using the actual $^{18}\text{O}_2$ isotopic fractions in the gas that was used during the first stage (g_1) and the second stage (g_2) of the experiment:³⁸

$$ir_{18} = \frac{if_{18} - g_1}{g_2 - g_1} \quad (1)$$

Nevertheless, also the calculation of if_{18} values can provide misleading results for measurement points with comparably low intensities for both distinguished oxygen isotopes. Thus, the application of Eq. (1) for measurement points that exhibit ($^{18}\text{O}^-$)-($^{16}\text{O}^-$) value pairs of 3–1 and 6–2, respectively, would both lead to the same result. Undoubtedly, the second measurement has higher relevance to the desired conclusions on transport mechanisms in the grown oxide scales. To overcome the above described difficulties for low-intensity values, measurement points

exhibiting both $^{18}\text{O}^-$ and $^{16}\text{O}^-$ intensities below a certain threshold were treated as 0. The thresholds for oxygen ion intensities were individually determined for each experiment.

Foss et al.³⁹ used if_{18} maps following two-stage oxidation of a commercial Ni-base Superalloy to calculated ‘pseudo’-depth profiles of if_{18} intensities. The underlying principle was already presented earlier²⁹ and is slightly adapted in this study. For the calculation of \bar{if}_{18} , depending on the penetration depth x of oxygen into the scale, the values from one row were summed and divided by the total number of considered columns N :

$$\bar{if}_{18}(x) = \frac{1}{N} \sum_{i=1}^n if_{18} \quad (2)$$

Due to the irregular outer oxide interface, usage of the average if_{18} across the entire width of the displayed oxide scale overestimates the expansion of d_1 . The calculation of if_{18} depth profiles from sections where the outer oxide scale is nearly parallel to the initial sample surface can be demonstrated to be considerably more meaningful. Isotopic enrichment depth profiles (IEDPs) from the sections marked in Fig. 7d–f were calculated using Eq. (2) and are summarised in Fig. 8.

Enrichment profiles of ternary Co-base model alloys after two-stage exchange experiments at 900 °C exhibit significant \bar{if}_{18} values at the outer scale interface and the IOF. $^{18}\text{O}^-$ maps indicate a comparable distribution of marked oxide phases over all oxide scales that were analysed after 24 h tracer exposure at 900 °C. As already described above, counter-current transport mechanisms are confirmed for ternary Co-base model alloys irrespective of the W content. However, more specific indications on the prevailing nature of oxygen transport through the internal oxidation zone can be extracted from the displayed figure. For all elucidated compositions, the computed IEDPs indicate a considerable enrichment of $^{18}\text{O}^-$ at the transition from d_2 to d_3 after two-stage tracer exchange experiments at 900 °C. The sample that contains the lowest W level exhibits this zone between 50 and 60 μm below the outer oxide interface. The only valid explanation for this rise in labelled oxygen is the oxidation of phases in the former zone of internal precipitates embedded in the matrix. In other words, there is an additional oxidation front following the progress of the IOF into the sample. For 9Wsx, two significantly different sections of the outer oxide scale were considered for the calculation of if_{18} depth profiles. The first region of the scale, Fig. 7b, exhibits apparent indications for transport of oxygen along a grain boundary in the outer oxide layer. High isotopic enrichment is evident over the first 7 μm (Fig. 8b). After this, the computed pseudo depth profile exhibits features of a classical concentration profile developed during diffusion in a semi-infinite media. Increased \bar{if}_{18} values on the edge of a pore, above the original sample surface, caused the sharp peak between 19 and 20 μm. Towards the internal precipitation region, a moderate increase can be observed. Higher average intensities due to more extensive SI yields of Al-containing oxide phases might considerably contribute to the computed \bar{if}_{18} values in d_2 . The second region of the multilayered oxide on 9Wsx, Figs 7b and 8c, was deliberately chosen to represent the interior of one large grain of d_1 . Contrary to the first profile, no indications of considerable oxygen transport via diffusion can be found in d_1 . Three sharp peaks of \bar{if}_{18} between 20 and 30 μm are caused by newly grown oxide inside the pores of the outer oxide layer. Separation of two independently progressing oxidation fronts is less obvious but still recognisable in the IEDP ($x > 47$ μm) of region O2 (Fig. 8c). The sample with the highest W content demonstrates particularly low ^{18}O intensity in the transition zone from the inner oxide layer to the internal precipitation region (Fig. 8d). The calculated values of \bar{if}_{18} stay negligibly low over ~5 μm and undergo a moderate increase in the upper region of d_3 . During the investigation of samples that were oxidised in synthetic air with field emission

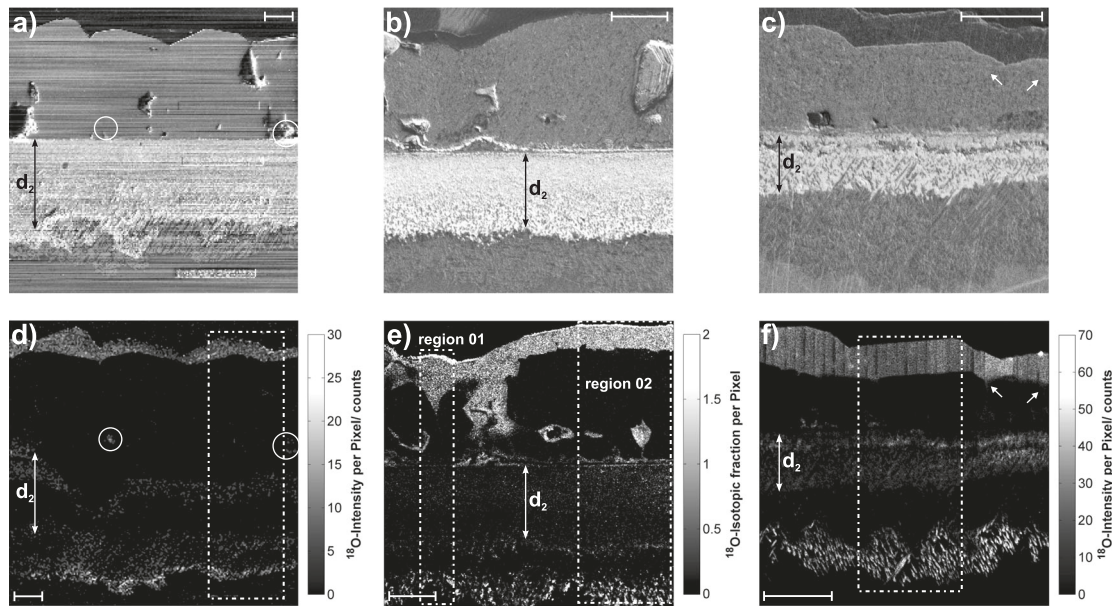


Fig. 7 Total positive secondary ion images and $^{18}\text{O}^-$ intensity maps of ternary Co-base model alloys after 24 h tracer exchange experiments at 900 °C. Displayed are cross-sections of multilayered oxide scales on (a) 7Wsx, (b) 9Wsx and (c) 10Wsx. **d–f** The corresponding SIMS intensity maps represent the distribution of labelled oxygen ($^{18}\text{O}^-$) after 8 h exposure. See the text for the explanation of white circles, arrows and the marked regions. Scale bars, 10 μm

scanning electron microscopy, no evident porosity was observed in d_3 . Consequently, the Al-depleted matrix surrounding the Al_2O_3 phases must remain widely unaffected during oxygen transport through this zone in the second oxidation stage.

BSE micrographs in accordance with data of thermogravimetric exposure indicated significantly slower penetration of oxygen during scale growth at 850 °C and 800 °C on 9Wsx. Furthermore, the oxidation kinetics at 900 °C were demonstrated to undergo considerable alterations already during the first 5 h of exposure.²¹ To verify whether experimental time at 900 °C or lower oxidation temperature can be attributed to alterations in the predominating transport mechanisms, additional two-stage oxidation experiments were conducted with 9Wsx samples. A further tracer exchange experiment was performed for 5 h with the same composition at 900 °C. Figure 9 displays SI micrographs of 9Wsx after 24 h two-stage oxidation at 800 °C and 850 °C, and 5 h at 900 °C along with corresponding $^{18}\text{O}^-$ distribution maps.

In order to minimise sputter damage during SIMS analysis, primary ion beam currents require careful selection. It has to be noted that the investigated section of the oxide scale after exposure at 800 °C is ~ 5 times smaller than those displayed for experiments at higher temperatures (compare Fig. 9b, c). Smaller ion beam currents are mandatory for the investigation of relatively thin oxide layers, which consequently leads to a lower SI yield. These adjustments are inevitably reflected in low $^{18}\text{O}^-$ signals. The calculations of IEDP after tracer exchange experiments for shorter times and lower temperatures therefore do not reach the significance of the results presented in Fig. 8 and are therefore not displayed. After 800 °C, the appearance of significant $^{18}\text{O}^-$ signal (Fig. 9d) also accounts for simultaneous transport of cations to the outer interface and oxygen to the IOF. The distribution of labelled oxide in d_1 is less localised compared with higher temperatures. Analogous to the results for the lowest considered temperature, oxide phases that reveal the marked oxygen isotope after 24 h at 850 °C are evident on the alloy/scale interface and throughout d_1 (see Fig. 9d). For both exposures below 900 °C, the ^{18}O -containing cobalt oxide is not limited to a narrow region at the topmost sections of d_1 . Oxide scales after short-term tracer exchange exposure at 900 °C (Fig. 7f) however exhibits similar

$^{18}\text{O}^-$ distribution tendencies than the one obtained after longer durations (Fig. 7e). Considerable amounts of labelled oxides are evident at the external and internal scale interfaces. Minor enrichment of $^{18}\text{O}^-$ is apparent around small pores in the outer oxide layer. Intermediate signal of labelled oxides is also detected in the inner oxide layer. Furthermore, the measured $^{18}\text{O}^-$ intensity is almost completely spread over d_3 .

DISCUSSION

In the following, the above presented findings that can be directly correlated to material transport during oxidation of Co-base model alloys with the nominal composition $\text{Co}_9\text{Al}_x\text{W}$ ($x = 8, 9, 10$ at.%) in the transient stages of scale growth between 800 °C and 900 °C are discussed in detail. For a more complete picture on the composition of multilayered oxide scales, the development of oxidation kinetics during 100 h experiments as well as the evolution of Al-containing barrier layers, the reader is referred to our already published study.³⁵

The results obtained after two-stage oxidation experiments revealed similar transport mechanisms for all considered ternary Co-base model alloys between 800 °C and 900 °C. Counter-current transport of reactants through the growing scale is evident in each of the elucidated samples. For ternary Co-base model alloys, d_1 is assumed to be almost exclusively composed of CoO at 850 °C and 900 °C. In recent studies on the oxidation behaviour of polycrystalline Co-base Superalloys, considerable quantities of Co_3O_4 were found in the outer oxide layers after exposure at 800 °C.^{15,19} These findings are in reasonable accordance with literature on the oxidation mechanisms of pure cobalt and its alloys. As indicated by BSE micrographs (Fig. 2) and measurements of individual layer thicknesses (Fig. 6), the expansion of d_1 has a significant impact on the overall kinetics of scale formation characterised during thermogravimetry (Fig. 1) at 900 °C for 24 h.

The observed coarsening of grains in the CoO layer on 9Wsx during oxidation at 900 °C is an indication for relatively rapid transport processes. Several renowned studies discussed the evolution of the so-called duplex oxide films on metals and binary alloys.^{40–42} Such oxide layers are reported to consist of epitaxial

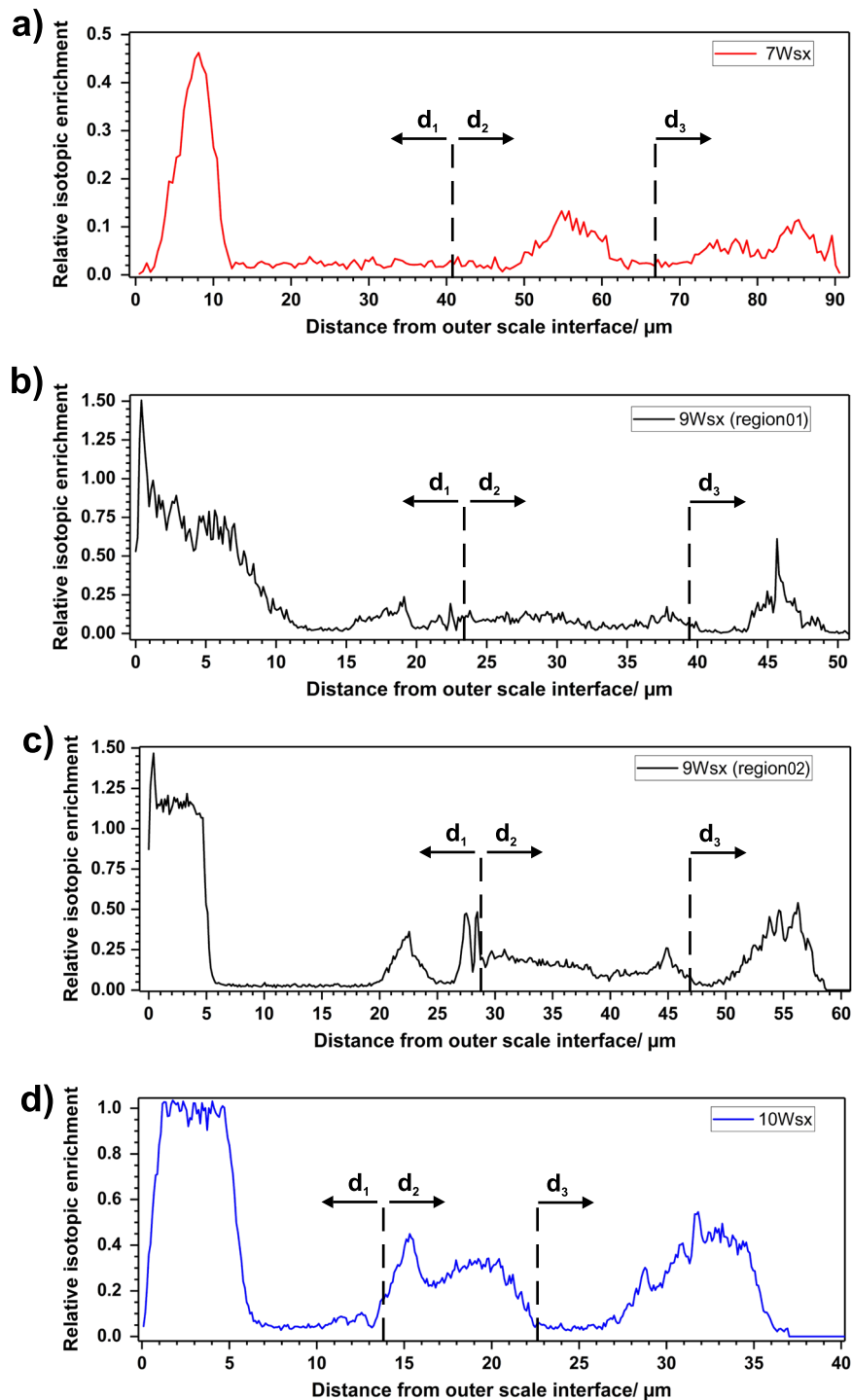


Fig. 8 Average IEDP of ternary alloys with varying W content after 24 h two-stage oxidation experiments at 900 °C. The profiles were calculated Eq. (2) from sections marked in Fig. 7

grains, which are subsequently overgrown by large columnar grains. In the upper region of the duplex scales at 900 °C, no preferential orientation was found (compare Figs 3 and 4). Following Atkinsons model predictions, rapid outward transport of cations and high exposure temperatures essentially contribute to the development of duplex structures in outward expanding oxide layers.³⁷ The dependency of grain size on oxidation temperature was clearly demonstrated by the investigation of grain structures on ternary Co-base model alloys in the EBSD analysis (Figs 4 and 5c, d) presented in this study. The specific

impact of W on the scale growth of high-temperature alloys are rarely conducted in a systematical manner. However, a comparison of the oxidation behaviour of two Co-Cr-W alloys with 1.3 and 2.6 at.% W can be found in the literature.⁴³ Reduced mass gain of samples with higher W levels during the early stages of scale formation at 1050 °C was reported. In the present study, the oxidation behaviour of ternary Co-base alloys at 900 °C exhibits a similar dependency on increasing W content. Differences in the growth kinetics also cause variations in the thickness of outer oxide layers that clearly decreases with increasing W levels (Fig. 6).

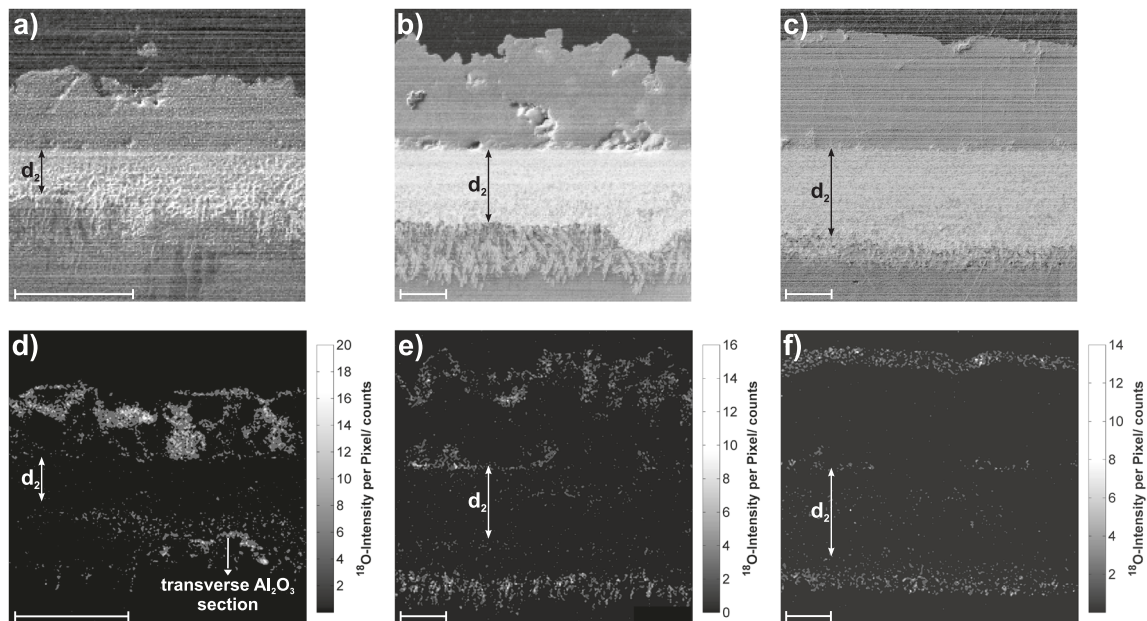


Fig. 9 Total positive secondary ion images and $^{18}\text{O}^-$ intensity maps after tracer exchange experiments of 9Wsx. Displayed are cross-sections after a total 24 h exposure at (a) 800 °C and (b) 850 °C. d, e The corresponding SIMS intensity maps represent the distribution of labelled oxygen ($^{18}\text{O}^-$) after 8 h exposure. c, f Total positive secondary ion image along with $^{18}\text{O}^-$ distribution map of 9Wsx after 5 h tracer exchange experiment at 900 °C. Scale bars, 5 μm

In general, the formation of defects in externally grown oxide layers on Co is correlated to increased temperature and/or oxygen partial pressures.⁴⁴ Differences in growth kinetics of single-phase oxides are often explained by prevailing defect densities in the respective layers. Altered defect properties in d_1 on ternary Co-base alloys that are dependent on the W levels in the sample are hardly conceivable. In other words, the outward expansion of d_1 on ternary Co-base alloys is comparable to oxide growth characteristics of pure Co at high temperatures and not significantly influenced by the W content in the alloy system. EBSD mappings after 24 h support this assumption, even though the development of layer thickness was not presented in detail for W levels of 7 and 10 at.%. Instead, transport properties of Co to the original alloy surface are supposed to be lowered by the increasing W content in the alloy. Consequently, after the onset of considerable diffusion of the base element from the alloy, the activity of Co at the d_1/d_2 interface decreases slower for samples exhibiting higher W levels. This can also explain the observed changes in oxidation kinetics caused by the variations of the W contents in the ternary model system. However, to prove the validity of this statement, more information of the development of individual layer thicknesses for 7Wsx and 10Wsx in the considered temperature range are needed.

Figure 10 schematically illustrates the enrichment of ^{18}O -containing oxide after a 24 h two-stage oxidation experiments. For easier allocation of the transport processes that are discussed in the following section, the SIMS intensity distribution maps of samples with 9 or 10 at.% W after exposure to 900 °C (Fig. 7e, f) were chosen as the basis for the schematic drawing. Nevertheless, the indicated features are relevant for all samples that were investigated by means of two-stage tracer exchange experiments.

Exclusive grain-boundary diffusion of mainly oxygen was reported for commercial Ni- or Fe-base alloys that grow an external alumina layers.^{45,46} Due to the substantial amount of newly formed oxide phases in the internal oxidation zone that was observed in this study, the sole transport of oxygen by diffusion along grain boundaries seems improbable. Atkinson et al.⁴⁷ investigated the outward expansion of NiO layers by means of tracer exchange studies. In their study, the authors concluded that

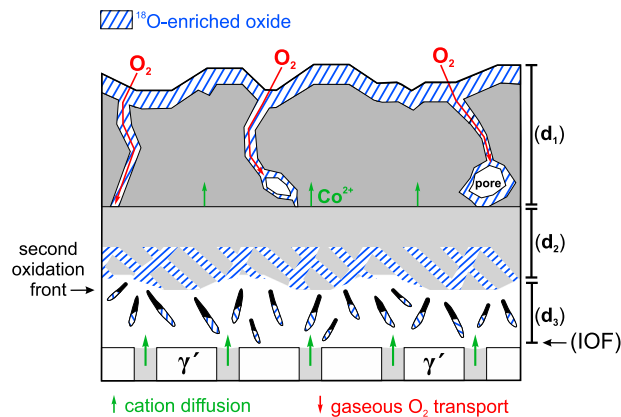


Fig. 10 Schematic representation of ^{18}O distribution in multilayered oxide scales on ternary Co-base model alloys after two-stage tracer exchange experiments. Directly derived paths for material transport are indicated as arrows

short-circuit diffusional transport of anions along grain boundaries cannot explain the penetration rate of oxygen in the considered temperature regime. The conclusion that microcracks during the evolution of duplex grain structures in external NiO layers might provide direct access for O_2 was also discussed in further publications.^{48,49} Even though the pore structure of d_1 was not subject of the presented investigations, the insufficient resistance against internal oxidation for all investigated ternary alloys at 900 °C can be attributed to the observed porosity in the outer oxide layer. To avoid a speculative interpretation of the results from two-stage tracer exchange experiments, discussion in the following is mostly restricted to unambiguous mechanistic findings in the outer oxide layer.

Chen et al.⁵⁰ demonstrated the diffusion of Co to be several orders of magnitude faster than diffusion of O in CoO at a given temperature. Therefore, the extensive transport of oxygen towards the IOF cannot be sustained by diffusion through d_1 . Instead, a possible explanation is the evolution of so-called microchannels in

the outer oxide layer. Kofstad and Hed^{40,51} discussed the role of porosity in CoO layers grown on binary Co-Cr alloys during exposure between 800 °C and 1300 °C. In these studies, the development of a pore network was postulated to enable rapid transport of molecular oxygen. The first systematic investigation of oxygen transport through microchannels was provided for the oxidation of Fe-Cr alloys at 1000 °C.²⁶

The underlying theory follows well-known models of crack formation that occurs in fast expanding oxide layers.^{41,52,53} In the referred studies, the evolution of microchannels is postulated to start with extensive depletion of metal. After considerable accumulation of metal vacancies, local-scale detachment above the considered interface can take place. The growth of the fine-grained inner scale section is reported to correspond to localised events of scale spallation. Sheasby and Gleeson⁵⁴ supported the aforementioned model prediction for the scale formation on Co with oxygen tracer studies between 1000 °C and 1300 °C. However, new oxide phases were located around grain boundaries in the columnar section of d_1 for 9Wsx and 10Wsx after 24 h two-stage tracer exposure at 900 °C (see Fig. 7). The formation of labelled oxide in regions that surround microchannels can be interpreted as lattice expansion instead of an indication for diffusion of oxygen along grain boundaries. This is in good agreement with tracer exchange experiments on pure Co at elevated temperatures.⁵⁴

Two significant segments of ¹⁸O tracer enrichment can be distinguished in the internal oxidation zones ($d_2 + d_3$) of all investigated Co-base model alloys. Besides newly formed oxide phases on the IOF, the regions above the d_2/d_3 interface exhibit considerable ¹⁸O⁻ intensities. The latter finding is further evidence for the existence of a second oxidation front that was already demonstrated in a previous study on the high-temperature oxidation of a ternary Co-base model alloys at 900 °C.²¹ From the set of presented data, it cannot be stated whether gaseous oxygen penetrates deeper than the original alloy surface. X-ray or FIB tomography might be suitable techniques to further elucidate pore networks in the inner oxide layer.⁵⁵ For tracer exposures of 24 h, d_3 is separated into two parts that formed during the subsequent stages of oxidation. Directly below the d_2/d_3 interface, the internal alumina precipitates exhibited no ¹⁸O⁻ intensities, whereas labelled oxide phases were evident directly above the IOF. No apparent porosity was observed in d_3 . Therefore, the possibility of molecular oxygen transport through d_3 can most probably be excluded. As only Al₂O₃ was found in this region, also opportunities for preferential oxygen diffusion paths are limited. A possible explanation is the diffusion of oxygen along the incoherent interfaces between precipitates and surrounding substrate. An analogous mechanism was also postulated for binary NiAl systems.^{56,57}

The duplex structures that were extensively investigated on binary Ni alloys during thermal exposure exhibited a clear tendency towards smaller grain sizes at lower oxidation temperatures.⁵⁸ This is in good agreement with the presented grain structures of outer oxide layers on ternary Co-base model alloys after 24 h thermogravimetry at 800 °C and 850 °C (Fig. 5c, d). Despite the overall smaller grains, considerable porosity was still evident in outer oxide layers that developed at 800 °C and 850 °C. Therefore, the molecular transport of oxygen via microchannels is also conceivable in this temperature range. The ratio of inner-pore surface to outer-oxide interface increases for finer grain structures. Furthermore, slower cation diffusion due to lower exposure temperatures enhances the probability of metal–oxygen interaction on the pore surfaces. These considerations can explain the significant traces of labelled oxide phases in the interior of d_1 after exposure at 800 °C and 850 °C, as can be seen in Fig. 9d, e.

Elementary mechanisms during the transient oxide scale growth on ternary Co-base model alloys with varying W levels were investigated between 800 °C and 900 °C. A deliberately

Table 1. Chemical composition (at.%) of the investigated ternary Co-base model alloys

Designation	Nominal composition	Measured composition		
		Co	Al	W
7Wsx	Co9Al7W	83.2	9.6	7.2
9Wsx	Co9Al9W	81.3	9.7	9.0
10Wsx	Co9Al10W	80.2	9.7	10.1

chosen combination of experimental strategies and advanced analysis techniques allowed a detailed elucidation of transport mechanisms through expanding multilayered oxide scales and lead to the following conclusions:

1. Grain coarsening during the rapid expansion of the outer oxide layer was exclusively observed for ternary model alloys at 900 °C.
2. Counter-current transport of Co cations and oxygen was evident for all investigated oxide scales after exposure in the considered temperature regime.
3. The presented combination of two-stage oxidation experiments and FIB-SIMS allows the identification of two reaction fronts in the internal oxidation zone. In addition, the potential of this experimental approach to elucidate transitions in oxidation stages was indicated.
4. Usage of tracer exchange experiments unambiguously confirmed the development of microchannels in the outer oxide layer of all investigated alloys at high temperatures.
5. During transient oxidation of ternary Co-base model alloys, higher W concentration and lower exposure temperatures lead to slower Co diffusion in the alloy, without altering the transport mechanisms in the outer oxide scale.

Results for the oxidation of the considered ternary Co-base Superalloys at high temperatures were validated with classical theories describing the formation of duplex scales or material transport mechanisms during scale growth on comparable model systems.

METHODS

Manufacturing and preparation of samples

Three rod-shaped single-crystals were cast in a Bridgman investment casting facility at the Institute of Metals Science and Technology (WTM, University of Erlangen-Nürnberg (FAU), Germany). All samples revealed a two-phase microstructure after a heat treatment that consists of homogenisation at 1300 °C and subsequent aging at 900 °C for up to 200 h in a vacuum furnace. To determine the actual compositions, pieces of each ternary system were dissolved and subsequently investigated by inductively coupled plasma emission spectrometry. Results along with individual designation used in the course of this work are given in Table 1. Prior to thermal exposure, all relevant surfaces of disc-shaped samples with ~0.8 mm height were ground and polished down to 1 µm surface finish.

Thermogravimetric analysis

Thermogravimetry was performed using a Setaram Evolution 1650 analyser under constant gas flow of 20 cm³/min. The atmosphere inside the reaction tube was argon during heating. At the target temperature, the interior of the device was evacuated and refilled with dry synthetic air (80% N₂ + 20% O₂). The detection of mass gain during isothermal oxidation experiments started with the admission of the oxidising gas.

Two-stage oxidation experiments

Samples were placed on a weighing boat in a quartz tube. Prior to the experiment, the system is evacuated to a pressure below 1×10^{-6} mbar.

The tube is filled with normal oxygen. The furnace is heated at a constant rate to the target temperature and is rolled on the quartz tube. As soon as the target temperature is reached, the first ^{16}O step starts. As recently demonstrated, oxidation kinetics of ternary Co-base model alloys reach a quasi-steady state beyond 12 h exposure. Therefore, except for one short-term experiment, the duration of exposure $t_{16\text{O}}$ in natural oxygen was chosen to last 16 h. The ^{18}O isotopic fraction of the gas that was used for the second step varied between 0.540 and 0.494, well above the natural abundance of ^{18}O at 0.02. Exposure in ^{18}O -enriched atmosphere was always conducted for half of the duration of $t_{16\text{O}}$.

Preparation of oxide-scale cross-sections

All oxidised samples were protected by an electrochemically deposited Ni layer to minimise spallation loss during further metallographic preparation. High quality of each cross-section is essential and is achieved by argon ion-milling with the Hitachi IM4000 system for surface finishing prior to analysis in a field-emission scanning electron microscope (Hitachi FE-SEM S-4800) and to obtain clear EBSD pattern. Distances were directly determined from the BSE micrographs with the imaging software ImageJ. The metallographic preparation of samples was slightly modified for the acquisition of oxidised alloys using the FIB-SIMS. In these cases, the Ni-coated samples were embedded in epoxy resin and conventionally polished to 1 μm finish.

Secondary ion mass spectroscopy

A FEI-FIB200-SIMS instrument was used for the SIMS investigations on cross-sections after two-stage tracer exchange experiments. The instrument base pressure is below 1×10^{-7} mbar. The FEI quadrupole-based SIMS detector is set up to detect the negative oxygen SIs. A gridded channeltron detector was used for gallium beam-generated secondary electron and SI images of the analysed sample regions. The $^{16}\text{O}^-$ SIMS map was always recorded prior to the $^{18}\text{O}^-$ SIMS map. An eight times higher ion beam dwell time per pixel for the acquisition of $^{18}\text{O}^-$ SIMS maps was necessary to enable comparable intensity levels for the two detected oxygen isotopes. More details on the experimental procedures and especially the conducted SIMS analysis of cross-sections after two-stage tracer exchange experiments can be found elsewhere.^{31,59}

DATA AVAILABILITY

The data that supports the results of the present study are available from the corresponding author upon request.

Received: 27 June 2019; Accepted: 9 September 2019;

Published online: 30 September 2019

REFERENCES

- Reed, R. C. *The Superalloys: Fundamentals and Applications* (Cambridge Univ. Press, 2008).
- Sims, C. T., Stoloff, N. S. & Hagel, W. C. *Superalloys II: High-Temperature Materials for Aerospace and Industrial Power* (John Wiley & Sons, 1987).
- Gell, M., Duhl, D. N. & Giamei, A. F. The development of single crystal superalloy turbine blades. In *Superalloys 1980: Proceedings of the 4th International Symposium on Superalloys* 205–214 (1980).
- Pieraggi, B. & Dabosi, F. High-temperature oxidation of a single crystal Ni-base superalloy. *Werkst. Korros.* **38**, 584–590 (1987).
- Wagner, C. Reaktionstypen bei der Oxydation von Legierungen. *Z. für Elektrochemie, Ber. der Bunsenges. für physikalische Chem.* **63**, 772–782 (1959).
- Wagner, C. Passivity and inhibition during the oxidation of metals at elevated temperatures. *Corros. Sci.* **5**, 751–764 (1965).
- Hagel, W. C. The oxidation of iron, nickel and cobalt-base alloys containing aluminum. *Corrosion* **21**, 316–326 (1965).
- Wagner, C. Theoretical analysis of the diffusion processes determining the oxidation rate of alloys. *J. Electrochem. Soc.* **99**, 369–380 (1952).
- Mortazavi, N. et al. Interplay of water and reactive elements in oxidation of alumina-forming alloys. *Nat. Mater.* **17**, 610–617 (2018).
- Dryepontd, S., Turan, J. C., Lance, M. J. & Pint, B. A. 3D microscopy to assess the effect of high temperature cyclic oxidation on the deformation of cast and ODS FeCrAlY alloys. *Oxid. Met.* **91**, 327–347 (2019).
- Pint, B. A., DiStefano, J. R. & Wright, I. G. Oxidation resistance: one barrier to moving beyond Ni-base superalloys. *Mater. Sci. Eng. A* **415**, 255–263 (2006).
- Sato, J. et al. Cobalt-base high-temperature alloys. *Science* **312**, 90–91 (2006).
- Suzuki, A. & Pollock, T. M. High-temperature strength and deformation of γ/γ' two-phase Co-Al-W-base alloys. *Acta Materialia* **56**, 1288–1297 (2008).
- Bauer, A., Neumeier, S., Pyczak, F. & Göken, M. Microstructure and creep strength of different γ/γ' -strengthened Co-base superalloy variants. *Scr. Materialia* **63**, 1197–1200 (2010).
- Klein, L., Shen, Y., Killian, M. S. & Virtanen, S. Effect of B and Cr on the high temperature oxidation behaviour of novel γ/γ' -strengthened Co-base superalloys. *Corros. Sci.* **53**, 2713–2720 (2011).
- Klein, L., Bauer, A., Neumeier, S., Göken, M. & Virtanen, S. High temperature oxidation of γ/γ' -strengthened Co-base superalloys. *Corros. Sci.* **53**, 2027–2034 (2011).
- Yeh, A.-C., Wang, S.-C., Cheng, C.-F., Chang, Y.-J. & Chang, S.-C. Oxidation behaviour of Si-bearing Co-based alloys. *Oxid. Met.* **86**, 99–112 (2016).
- Klein, L., Killian, M. S. & Virtanen, S. The effect of nickel and silicon addition on some oxidation properties of novel Co-based high temperature alloys. *Corros. Sci.* **69**, 43–49 (2013).
- Yan, H.-Y., Vorontsov, V. A. & Dye, D. Effect of alloying on the oxidation behaviour of Co-Al-W superalloys. *Corros. Sci.* **83**, 382–395 (2014).
- Pettit, F. S. Oxidation mechanisms of nickel-aluminium alloys at temperature between 900° and 1300 °C. *Trans. Metall. Soc. AIME* **239**, 1296–1305 (1967).
- Weiser, M., Eggeler, Y. M., Spiecker, E. & Virtanen, S. Early stages of scale formation during oxidation of γ/γ' strengthened single crystal ternary Co-base superalloy at 900 °C. *Corros. Sci.* **135**, 78–86 (2018).
- Ooshima, M., Tanaka, K., Okamoto, N. L., Kishida, K. & Inui, H. Effects of quaternary alloying elements on the γ' solvus temperature of Co-Al-W based alloys with fcc L_{12} two-phase microstructures. *J. Alloy. Compd* **508**, 71–78 (2010).
- Pyczak, F. et al. The effect of tungsten content on the properties of L_{12} -hardened Co-Al-W alloys. *J. Alloy. Compd* **632**, 110–115 (2015).
- Stewart, C. A., Suzuki, A., Pollock, T. M. & Levi, C. G. Rapid assessment of oxidation behavior in Co-based γ/γ' alloys. *Oxid. Met.* **90**, 485–498 (2018).
- Weiser, M. et al. Influence of Co to Ni ratio in γ' -strengthened model alloys on oxidation resistance and the efficacy of the halogen effect at 900 °C. *Corros. Sci.* **156**, 84–95 (2019).
- Brückman, A., Emmerich, R. & Mrowec, S. Investigation of the high-temperature oxidation of Fe-Cr alloys by means of the isotope ^{18}O . *Oxid. Met.* **5**, 137–147 (1972).
- Basu, S. N. & Halloran, J. W. Tracer isotope distribution in growing oxide scales. *Oxid. Met.* **27**, 143–155 (1987).
- Jedlinski, J. & Borchardt, G. On the oxidation mechanism of alumina formers. *Oxid. Met.* **36**, 317–337 (1991).
- Chater, R. J., Carter, S., Kilner, J. A. & Steele, B. C. H. Development of a novel SIMS technique for oxygen self-diffusion and surface exchange coefficient measurements in oxides of high diffusivity. *Solid State Ion.* **53–56**, 859–867 (1992).
- Ooi, T. N., McPhail, D. S., Chater, R. J. & Shollock, B. A. Isotope exchange studies of oxidation mechanisms in nickel-base superalloys using FIB-SIMS techniques. *Surf. Coat. Technol.* **201**, 3885–3888 (2006).
- Chater, R. J., Weiser, M. & Virtanen, S. Visualizing ion transport mechanisms through oxide scales grown on mixed nickel- and cobalt-base model alloys at 900 °C using FIB-SIMS techniques. *J. Vacuum Sci. Technol. B* **36**, 03F116 (2018).
- Göbel, M., Rahmel, A. & Schütze, M. The isothermal-oxidation behavior of several nickel-base single-crystal superalloys with and without coatings. *Oxid. Met.* **39**, 231–261 (1993).
- Naumenko, D., Quadackers, W. J., Galerie, A., Wouters, Y. & Jourdain, S. Parameters affecting transient oxide formation on fecral based foil and fibre materials. *Mater. High. Temp.* **20**, 287–293 (2003).
- Sato, A., Chiu, Y.-L. & Reed, R. Oxidation of nickel-based single-crystal superalloys for industrial gas turbine applications. *Acta Materialia* **59**, 225–240 (2011).
- Weiser, M. & Virtanen, S. Influence of W content on the oxidation behaviour of ternary γ' - strengthened Co-based model alloys between 800 and 900 °C. *Oxid. Metals* (2019). in press.
- Atkinson, A., Taylor, R. I. & Hughes, A. E. A quantitative demonstration of the grain boundary diffusion mechanism for the oxidation of metals. *Philos. Mag. A* **45**, 823–833 (1982).
- Atkinson, A. Transport processes during the growth of oxide films at elevated temperature. *Rev. Mod. Phys.* **57**, 437–470 (1985).
- Alibhai, A. A., Chater, R. J., McPhail, D. S. & Shollock, B. A. Use of isotopic tracers and SIMS analysis for evaluating the oxidation behaviour of protective coatings on nickel based superalloys. *Appl. Surf. Sci.* **203–204**, 630–633 (2003).
- Foss, B. J., Hardy, M. C., Child, D. J., McPhail, D. S. & Shollock, B. A. Oxidation of a commercial nickel-based superalloy under static loading. *JOM* **66**, 2516–2524 (2014).

40. Kofstad, P. K. & Hed, A. Z. High-temperature oxidation of Co-10 w/o Cr alloys. *J. Electrochem. Soc.* **116**, 224–234 (1969).
41. Gibbs, G. B. & Hales, R. The influence of metal lattice vacancies on the oxidation of high temperature materials. *Corros. Sci.* **17**, 487–497 (1977). 499–507.
42. Hsu, H. S. & Yurek, G. J. Kinetics and mechanisms of the oxidation of cobalt at 600–800 °C. *Oxid. Met.* **17**, 55–76 (1982).
43. Karaali, A., Mirouh, K., Hamamda, S. & Guiraldenq, P. Effect of tungsten 0-8 wt.% on the oxidation of Co-Cr alloys. *Comput. Mater. Sci.* **33**, 37–43 (2005).
44. Fryt, E. Defect structure in CoO. *Oxid. Met.* **10**, 311–327 (1976).
45. Pint, B. A., Martin, J. R. & Hobbs, L. W. ¹⁸O/SIMS characterization of the growth mechanism of doped and undoped α -Al₂O₃. *Oxid. Met.* **39**, 167–195 (1993).
46. Naumenko, D., Gleeson, B., Wessel, E., Singheiser, L. & Quadackers, W. J. Correlation between the microstructure, growth mechanism, and growth kinetics of alumina scales on a FeCrAlY alloy. *Metall. Mater. Trans. A Phys. Metall. Mater. Sci.* **38A**, 2974–2983 (2007).
47. Atkinson, A., Taylor, R. I. & Goode, P. D. Transport processes in the oxidation of Ni studied using tracers in growing NiO scales. *Oxid. Met.* **13**, 519–543 (1979).
48. Atkinson, H. V. Evolution of grain structure in nickel oxide scales. *Oxid. Met.* **28**, 353–389 (1987).
49. Atkinson, H. V. Development of grain structure in nickel oxide scale. *Mater. Sci. Technol.* **4**, 1052–1063 (1988).
50. Chen, W. K., Peterson, N. L. & Reeves, W. T. Isotope effect for cation self-diffusion in CoO crystals. *Phys. Rev.* **186**, 887–891 (1969).
51. Kofstad, P. K. & Hed, A. Z. Oxidation of Co–25 w/o Cr at high temperatures. *J. Electrochem. Soc.* **116**, 1542–1550 (1969).
52. Mrowec, S. On the mechanism of high temperature oxidation of metals and alloys. *Corros. Sci.* **7**, 563–578 (1967).
53. Gibbs, G. B. A model for mild steel oxidation in CO₂. *Oxid. Met.* **7**, 173–184 (1973).
54. Sheasby, J. S. & Gleeson, B. Oxygen tracer study of the high-temperature oxidation of pure and impure cobalt. *Oxid. Met.* **32**, 379–390 (1989).
55. Fry, A. T., Gorman, D. M. & Brown, S. B. 3D evaluation of the oxidation and porosity in 9Cr tubing using FIB and X-ray. *Mater. High. Temp.* **35**, 2–13 (2018).
56. Whittle, D. P., Shida, Y., Wood, G. C., Stott, F. H. & Bastow, B. D. Enhanced diffusion of oxygen during internal oxidation of nickel-base alloys. *Philos. Mag. A* **46**, 931–949 (1982).
57. Stott, F. H. et al. The transport of oxygen to the advancing internal oxide front during internal oxidation of nickel-base alloys at high temperature. *Solid State Ion.* **12**, 365–374 (1984).
58. Atkinson, H. V. A review of the role of short-circuit diffusion in the oxidation of nickel, chromium, and nickel-chromium alloys. *Oxid. Met.* **24**, 177–197 (1985).
59. Weiser, M. *Elementary Mechanisms During the Early Stages of Scale Formation on Single Crystalline Co- and Ni-base Superalloys at High Temperatures*. PhD thesis (FAU Univ. Press, 2019).

ACKNOWLEDGEMENTS

Scientific and financial support by the Deutsche Forschungsgemeinschaft (DFG) through the Collaborative Research Center SFB-TR 103 (Project A5) is kindly acknowledged by M.W. and S.V. The present study was conducted as part of M.W.'s PhD project. Selected details were already included in MW's doctoral dissertation.

AUTHOR CONTRIBUTIONS

M.W. and S.V. planned the project. M.W. conducted all experiments, performed electron microscopic analysis, assisted SIMS measurements and wrote the initial manuscript in close consultation with S.V. R.J.C. acquired all SIMS data and gave important input for the presentation of results. B.A.S. provided access to the laboratory facilities at Imperial College and supervised the progress of two-stage tracer exchange experiments. All co-authors essentially contributed during reviewing of the final manuscript.

COMPETING INTERESTS

The authors declare no competing interests.

ADDITIONAL INFORMATION

Correspondence and requests for materials should be addressed to S.V.

Reprints and permission information is available at <http://www.nature.com/reprints>

Publisher's note Springer Nature remains neutral with regard to jurisdictional claims in published maps and institutional affiliations.



Open Access This article is licensed under a Creative Commons Attribution 4.0 International License, which permits use, sharing, adaptation, distribution and reproduction in any medium or format, as long as you give appropriate credit to the original author(s) and the source, provide a link to the Creative Commons license, and indicate if changes were made. The images or other third party material in this article are included in the article's Creative Commons license, unless indicated otherwise in a credit line to the material. If material is not included in the article's Creative Commons license and your intended use is not permitted by statutory regulation or exceeds the permitted use, you will need to obtain permission directly from the copyright holder. To view a copy of this license, visit <http://creativecommons.org/licenses/by/4.0/>.

© The Author(s) 2019